JACS
JOURNAL OF THE AMERICAN CHEMICAL SOCIETY
Article
pubs.acs.org/JACS

p-Type Transparent Conducting Oxide/n-Type Semiconductor Heterojunctions for Efficient and Stable Solar Water Oxidation

Le Chen,[†,‡] Jinhui Yang,[†,‡] Shannon Klaus,[†,∥] Lyman J. Lee,[†,‡] Rachel Woods-Robinson,[‡] Jie Ma,[†,‡] Yanwei Lum,[†,⊥] Jason K. Cooper,[†,⊥] Francesca M. Toma,[†,¶] Lin-Wang Wang,[†,‡] Ian D. Sharp,[†,§] Alexis T. Bell,[†,∥] and Joel W. Ager*[,†,‡]

[†]Joint Center for Artificial Photosynthesis, [‡]Materials Sciences Division, [¶]Chemical Sciences Division, and [§]Physical Biosciences Division, Lawrence Berkeley National Laboratory, Berkeley, California 94720, United States

[∥]Department of Chemical and Biomolecular Engineering and [⊥]Department of Materials Science and Engineering, University of California at Berkeley, Berkeley, California 94720, United States

Supporting Information

ABSTRACT: Achieving stable operation of photoanodes used as components of solar water splitting devices is critical to realizing the promise of this renewable energy technology. It is shown that p-type transparent conducting oxides (p-TCOs) can function both as a selective hole contact and corrosion protection layer for photoanodes used in light-driven water oxidation. Using $NiCo_2O_4$ as the p-TCO and n-type Si as a prototypical light absorber, a rectifying heterojunction capable of light driven water oxidation was created. By placing the charge separating junction in the Si using a np^+ structure and by incorporating a highly active heterogeneous Ni−Fe oxygen evolution catalyst, efficient light-driven water oxidation can be achieved. In this structure, oxygen evolution under AM1.5G illumination occurs at 0.95 V vs RHE, and the current density at the reversible potential for water oxidation (1.23 V vs RHE) is >25 mA cm^{-2}. Stable operation was confirmed by observing a constant current density over 72 h and by sensitive measurements of corrosion products in the electrolyte. *In situ* Raman spectroscopy was employed to investigate structural transformation of $NiCo_2O_4$ during electrochemical oxidation. The interface between the light absorber and p-TCO is crucial to produce selective hole conduction to the surface under illumination. For example, annealing to produce more crystalline $NiCo_2O_4$ produces only small changes in its hole conductivity, while a thicker SiO_x layer is formed at the n-Si/p-$NiCo_2O_4$ interface, greatly reducing the PEC performance. The generality of the p-TCO protection approach is demonstrated by multihour, stable, water oxidation with n-InP/p-$NiCo_2O_4$ heterojunction photoanodes.

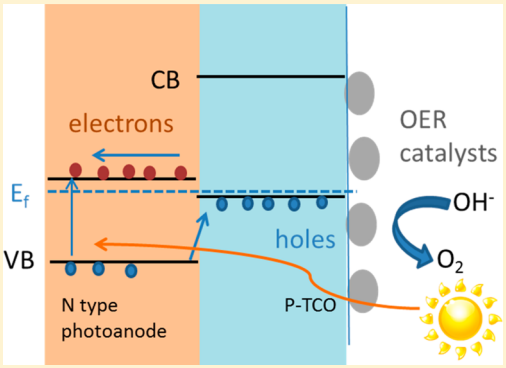

1. INTRODUCTION

The prospect of using sunlight directly to produce chemical fuels is attractive for providing alternatives to fossil fuels or enabling grid-scale energy storage, both of which are required for a more sustainable energy future.[1,2] Both hydrogen[3] and hydrocarbons[4] have been envisioned as sustainably produced solar fuels. One scheme to realize this type of direct solar to fuel conversion is to couple a tandem junction solar cell assembly, together with catalysts in a monolithically integrated device.[5−8] A typical design uses a p-type semiconductor as the photocathode, on which the target fuel is produced via reduction of protons to hydrogen or reduction of CO_2 to CO or hydrocarbon fuels. The sustained generation of these solar fuels requires a source of protons and electrons, which is provided by oxidation of water on a series-connected n-type semiconductor photoanode.

Fundamentally, several factors make this reaction difficult and demanding for materials selection of both the photoanode and photocathode. From a kinetic point of view, the water oxidation reaction is a challenging four-proton/four-electron process.[9] Additionally, stability is of primary concern for materials under water oxidation conditions, particularly at the extreme pH conditions that are used to ensure ion transport with minimal resistance losses in overall solar water splitting devices.[10] Indeed, in many of the earliest attempts to realize efficient solar water splitting with a tandem photovoltaic approach,[11] corrosion at the water oxidation photoanodes emerged as a critical issue which remains to this day.[12−14]

The stability criterion for semiconductor photoelectrodes under illumination was defined by Gerischer.[15] Briefly, a material is stable against corrosion in an electrolyte if its reductive and oxidative decomposition potentials lie in the conduction and valence bands, respectively. Conversely, if the decomposition potentials reside within the band gap, the material is unstable. Using this criterion, a recent *ab initio* study

Received: April 10, 2015
Published: July 10, 2015

ACS Publications © 2015 American Chemical Society

DOI: 10.1021/jacs.5b03536
J. Am. Chem. Soc. 2015, 137, 9595−9603

of a wide range of elemental and compound semiconductors found that only a small group of oxides, including TiO_2, Fe_2O_3, and Co_3O_4, are stable under illuminated water oxidation conditions.[16]

The prospect of integrating stable materials as protection layers on top of otherwise unstable photoanode materials is a potentially attractive approach to overcoming the limitations associated with corrosion.[14] Indeed, there were efforts in the 1970s and 1980s to protect III−V photoanodes with thin films of TiO_2; the key challenges which emerged from this work were creating a continuous coating to avoid failure at grain boundaries and tuning the oxide band structure to allow hole conduction to the solid/electrolyte interface.[11,17]

It is valuable to consider what would form an "ideal" protection layer. A first criterion is that it should form a continuous layer without pinholes or other flaws that could allow electrolyte contact to the underlying, unstable, photoactive material. Second, one would desire the transport of minority holes to the surface to be facile but the transport of majority carriers to be blocked. This will reduce the rate of interface recombination and thus promote an optimized photovoltage. Finally, for geometries in which the photoanode is illuminated from the front,[18] the protection layer should be transparent and possibly have antireflective properties, to maximize the carrier generation in the active material.[19]

Regarding the second criterion above, Campet et al.[20] have delineated the general possibilities for interfacial energetic alignment and associated charge transport, which are depicted schematically in Figure 1. In all cases, the n-type photoabsorber is coupled to a stable protective oxide with a higher conduction band edge, so as to create a barrier for electrons and reduce interface recombination of the photogenerated holes. Three possibilities are considered for hole transport to the surface. In the first case, the valence band of the protection layer is lower than that of the absorber, and holes are transported by tunneling, as shown in Figure 1a. This situation has been realized recently for water oxidation by Chen et al.[21] with thin layers of TiO_2 grown by atomic layer deposition on n-Si. Excellent stability under water oxidation conditions was achieved at pH 14. However, the thickness of the oxide layer needs to be carefully controlled, since the tunneling mechanism introduces a prohibitively large series resistance for films thicker than a few nm.[22,23]

The second case uses a protection layer which possesses a valence band below that of the absorber but allows hole transport through a defect band in the surface coating, as shown in Figure 1b. Such a system was demonstrated by Sun and Campet for protecting GaAs (though not for water oxidation) and allows the use of thicker protection layers.[24] This scheme was also realized recently for water oxidation by Hu et al.[25] using amorphous TiO_2 layers applied to a number of absorbers: n-Si, n-GaAs, and n-GaP. The protection layer could be as thick is 140 nm, ruling out a tunneling mechanism, and stabilities of over 100 h were demonstrated.

The third case is band conduction of holes in the protection layer, as illustrated in Figure 1c. This approach requires that the valence band of the protection layer be energetically aligned with or lie higher than that of the light absorber so that valence band hole transport can proceed without a barrier.[26] This approach has some potential advantages. For example, if the hole conduction through the layer is facile and the band gap is sufficiently large so as not to absorb visible light, the coating could be thicker and perhaps afford better corrosion protection.

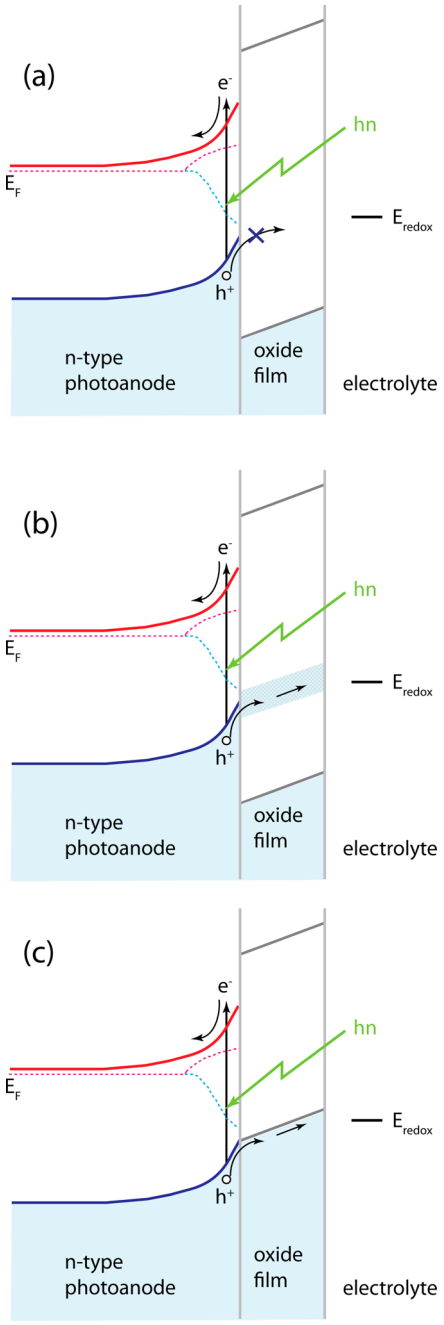

Figure 1. Schematic band diagram of hole transport through a protective oxide layer deposited on an n-type photoanode. Conduction and valence band edges are red and blue lines, respectively, and quasi-Fermi levels are indicated by dotted lines. Three mechanisms for hole transport are depicted: (a) tunneling, (b) defect band conduction, and (c) valence band transport. Adapted from Campet et al.[20]

These considerations in the third case provide promise for the use of p-type transparent conducting oxides (p-TCOs) as protection layers for water oxidation photoanodes. There has been significant recent work in developing p-TCOs for optoelectronics applications including organic light emitting diodes[26] and transparent electronics.[27] In general, the lower carrier conductivity of p-TCOs, (<100 S/cm),[28−30] compared to n-type TCOs (~10^4 S/cm range) such as indium tin oxide (ITO) has limited their commercial application in devices requiring lateral conductivity, such as solar cells.[31] However, as protection layers, out of plane charge transport occurs over

DOI: 10.1021/jacs.5b03536
J. Am. Chem. Soc. 2015, 137, 9595−9603

scales of 10s of nm, substantially shorter than the μm−mm scale needed for TCOs designed for in-plane transport. Therefore, the conductivity issues that have hindered p-TCOs in the past are less severe, and it is expected that some of these materials could be well suited for stabilization of semiconductors in solar fuel applications.

Indeed, there have been a number of recent reports using p-type oxide materials to protect otherwise unstable photoanode materials such as n-Si under illuminated water oxidation conditions in basic electrolytes (pH 13−14). For example, Yang et al.[32] found that atomic layer deposited thin films of CoO_x stabilized p^+-n Si in pH 14 electrolyte. However, the relatively narrow bandgap of CoO_x (E_g < 1.6 eV) leads to parasitic light absorption which limits the thickness of the coating to a few nanometers. There are a number of recent reports employing thin layers of p-type NiO. Sun et al.[33] used a semitransparent hole conducting ITO/Au/ITO layer coupling with an ultrathin NiO_x layer to protect n-Si and np^+-Si photoanode. Thicker NiO_x layers (50 to hundreds of nanometers) were used to stabilize np^+-Si photoanodes for hundreds to over 1000 h under water oxidation conditions.[34,35] However, there is a potential concern with NiO_x as the sole component of a protection scheme. During electrochemical cycling, as would occur during diurnal cycles in natural sunlight, NiO_x is known to convert to structurally porous $Ni(OH)_2$/NiOOH,[36−38] which ultimately could expose the vulnerable photoanode surface to the corrosive electrolyte.

In this study, we demonstrate the concept of a semiconductor corrosion protection based on band-edge transport, using $NiCo_2O_4$ as the p-type hole conducting material. $NiCo_2O_4$ has a smaller bandgap than NiO but higher than Co_3O_4 and has a hole conductivity (up to 300 S/cm) at least 2 orders of magnitude higher than either NiO or Co_3O_4.[39] It also crystallizes in the spinel structure similar to the less porous Co_3O_4. It has exceptional chemical stability in basic electrolytes and has been studied as an oxygen evolution (OER) catalyst and as an electrode in batteries and supercapacitors.[40−42] Many p-TCOs, including those in the well-studied delafossite family, require a high temperature step, >600 °C, for synthesis.[43−45] In contrast, $NiCo_2O_4$ can be synthesized at relatively low temperatures (100−400 °C) and thus can be integrated with a wide range of semiconductors, including Si and III-Vs.

In this work, we successfully applied $NiCo_2O_4$ as the hole conducting protection layer on Si and InP photoanodes. The holes generated in the light absorber are able to travel through the p-TCO layer and are effectively injected into the OER catalyst. The integrated water oxidation half-cell system demonstrated at least 72 h stability and one of the lowest onset potentials reported for an np^+-Si based photoanode for OER. We also investigate the role of the solid/solid interface between the light absorber and the p-TCO layer in achieving efficient carrier collection.

2. EXPERIMENTAL SECTION

A full description of the synthesis and characterization procedures is provided in the Supporting Information (SI); an overview will be given here. Commercially purchased single crystal Si and InP wafers were used for the light absorber components of the photoanodes; the surfaces of both are unstable under the illuminated water oxidation conditions employed. The np^+-Si structure was fabricated by ion implantation and rapid thermal annealing. The p-TCO, $NiCo_2O_4$, was deposited by reactive sputtering. A 40 nm layer of $NiCo_2O_4$ was found to provide both acceptable corrosion protection and optical transparency. The substrate was heated during deposition to ca. 70 °C. Other substrate temperatures were explored (see SI), but 70 °C was found to be optimal in terms of the PEC performance. Ni−Fe was used as an oxygen evolution catalyst; 2 nm films of this material were deposited by reactive cosputtering at room temperature. Up to 2 h of electrochemical cycling (0 to 0.7 V vs Hg/HgO, 10 mV/s) was performed on Ni−Fe coated samples to convert the metal Ni−Fe to the more OER-active Ni−Fe (oxy)hydroxide catalyst prior to testing. We note that the standard etch procedures to remove the native oxide on Si were not employed prior to p-TCO deposition; since the deposition is performed in an oxygen containing atmosphere in the presence of energetic ions, we found that some degree of SiO_x formation at the Si/p-TCO interface was unavoidable. The bulk of the photoelectrochemical (PEC) evaluations were performed with as-grown $NiCo_2O_4$ films. We also examined the critical role of the interface between the semiconductor light absorber and the p-TCO by annealing some samples at 400 °C in an inert atmosphere. Unless otherwise stated, PEC evaluations were performed with simulated AM1.5G illumination in aqueous solution at pH 14 in a standard three electrode cell.

In addition to standard thin film structural characterization techniques, including X-ray diffraction, electron microscopy, and scanning probe microscopy, we also employed methods which could yield information regarding the interfacial structure and energetics. These included depth-profiling X-ray photoelectron spectroscopy (XPS), measurement of the valence band edge by XPS, and evaluation of the work function of the $NiCo_2O_4$, by both XPS and *ab initio* calculations, and *in situ* analysis of the $NiCo_2O_4$ layer by Raman spectroscopy. We also used sensitive detection of corrosion products in the electrolyte using inductively coupled mass spectroscopy (ICP-MS) to evaluate the stability of the photoanode structures.

3. RESULTS AND DISCUSSION

3.1. Structural, Electronic and Optical Properties of Sputtered $NiCo_2O_4$ Thin Films. Transparency of an as-deposited 40 nm $NiCo_2O_4$ film on quartz was evaluated by looking at the transmission spectrum (Figure 2). At wavelengths >480 nm, the light transmission is >70%. The transmission increases to nearly 80% in the near-infrared, which corresponds to the locations of the bandgaps of Si (1.1 μm) and InP (950 nm). The p-type nature of the films was confirmed by the observation of positive Seebeck coefficients (Figure S5). A hole concentration in the low 10^{20} cm^{-3} range was measured by Hall effect. The valence band edge measured by XPS (Figure S23) is located very close to the surface Fermi

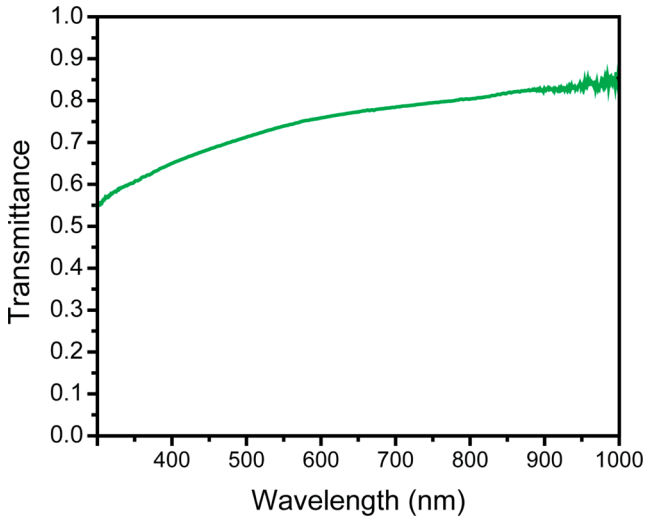

Figure 2. Transmittance spectrum of a 40 nm thick $NiCo_2O_4$ film sputter deposited onto an optically polished quartz wafer.

DOI: 10.1021/jacs.5b03536
J. Am. Chem. Soc. 2015, 137, 9595−9603

level, which is also consistent with a high, degenerate, hole concentration in the $NiCo_2O_4$. The hole conduction mechanism was found to be polaron hopping (Figure S6), as has been reported previously for $NiCo_2O_4$.[39] Nevertheless, the room temperature conductivity was in the range of 50−60 S/cm, which is comparatively high, particularly for a p-TCO deposited at near room temperature conditions.[29] If the $NiCo_2O_4$ film would be the only source of resistance between the light absorber and the electrolyte, we estimate a voltage loss of only 2 mV at 30 mA/cm^2 current density for a 40 nm thick film with a conductivity of 50 S/cm.

XPS survey scans of the as-deposited films identified the Ni to Co ratio as almost 1 to 2 (35:65), shown in Figure S22. The as-deposited films lacked long-range crystallinity as indicated by the absence of peaks in the X-ray diffraction (XRD) spectrum (Figure S1). To examine the crystalline structure more closely, $NiCo_2O_4$ and its interface with Si was studied by HR-TEM. Figure 3a shows that the as-deposited films are characterized by crystalline grains in the size regime of 2−4 nm. In comparison, postdeposition thermal annealing of the $NiCo_2O_4$ at 400 °C in argon yields larger and more prominent grains, as shown in Figure 3b. This result is consistent with corresponding XRD patterns, which reveal the emergence of crystalline peaks (Figure S1), and atomic force micrographs, which also exhibit a more granular morphology than the as grown samples (Figure S3).

In both as-deposited and annealed heterostructures, amorphous SiO_x layers are observed at the Si/p-TCO interface by HRTEM. The SiO_x layer at the as-grown $NiCo_2O_4$/Si interface is <2 nm thick, which is typical for a native oxide on Si. In contrast, the SiO_x layer at the annealed $NiCo_2O_4$/Si interface increases to a thickness of 3−4 nm. Further evidence of a thicker oxide layer was provided by depth-profiling XPS, as shown in Figure S25. Additionally, in Figure 3b, dark regions extend across the $NiCo_2O_4/SiO_x$ interface into the SiO_x layer which may be due to some amount of oxygen or metal atom diffusion.

3.2. Photoelectrochemical Evaluation of $NiCo_2O_4$ As a Hole Conducting Protection Layer on Si. For p^+-Si/p-$NiCo_2O_4$ junctions, we expect an ohmic contact due to high carrier concentration on both sides of the junction. This is demonstrated by the black curve in Figure 4a, which is a dark cyclic voltammogram (CV) scan of p^+ Si coated with 40 nm of $NiCo_2O_4$. The anodic current rises steeply from an onset near +1.6 V vs RHE, showing that the $NiCo_2O_4$ makes a low resistance contact to p^+-Si conducts into the electrolyte.

In order to provide further insights on the band diagram of our heterojunction, we used both theoretical calculations based on spin-polarized density functional theory (see Figure S26) and the measurement of secondary electron cutoff measured by XPS (Figure S24). The calculated work function is 4.42 eV, which is consistent with XPS measurement of 4.4 ± 0.1 eV. This places the Fermi level of the p-TCO within the bandgap of Si. A calculated band diagram is shown in Figure 5, the details of the calculation are provided in the SI. There is a modest amount of predicted upward band bending in the n-Si, implying that the junction should be rectifying. Indeed, this is observed in both photovoltaic (Figure S7) and PEC measurements. The blue curve in Figure 4a is the illuminated CV of a n-Si(100)/p-$NiCo_2O_4$ photoanode. There is a cathodic shift of the CV curve of about 150 mV compared to the p^+ Si/$NiCo_2O_4$ structure, which is consistent with the rectification predicted by the band diagram in Figure 5a. A saturation photocurrent density of more than 25 mA/cm^2 was achieved, demonstrating the efficient collection of minority carriers from the n-Si and their conduction through the 40 nm p-$NiCo_2O_4$ layer. The 24 h stability test results of $NiCo_2O_4$ on p^+ and n-Si are shown in Figures S8 and S9; the photocurrent is stable during the testing period.

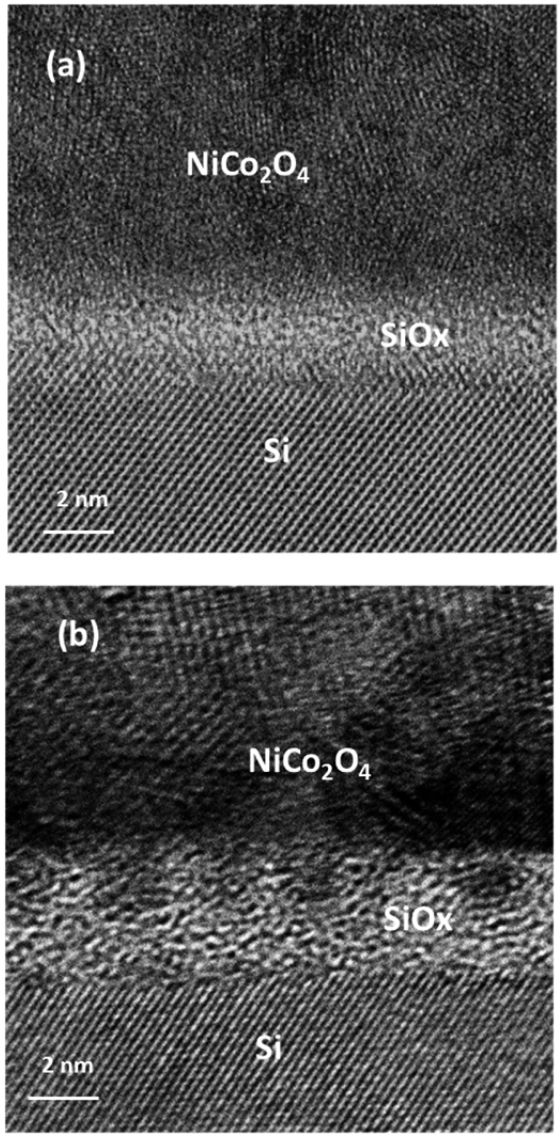

Figure 3. Cross-sectional TEM images of (a) as grown $NiCo_2O_4$/Si and (b) $NiCo_2O_4$/Si after annealing at 400 °C for 1 h in an inert atmosphere. The as-deposited $NiCo_2O_4$ has crystalline grains in the size regime of 2−4 nm; the grain size is increased with annealing. Annealing also increases the thickness of the SiOx layer from <2 to 3−4 nm.

In order to increase the cathodic shift of the onset potential, we employed n-Si with a p^+ emitter layer to provide additional built-in voltage. The simulated band diagram for this structure is shown in Figure 5b and the illuminated $J-V$ curve is shown in red in Figure 4a. The slope of photocurrent rise upon the onset is about the same as the $NiCo_2O_4$/n-Si and the saturation current is about 27 mA/cm^2. However, the onset potential for this system reduces to 1.05 V vs RHE, which makes the photocurrent density close to 10 mA/cm^2 at 1.23 V RHE (the water oxidation potential). In this structure, the function of the PV junction and the surface OER catalyst is decoupled,

DOI: 10.1021/jacs.5b03536
J. Am. Chem. Soc. 2015, 137, 9595−9603

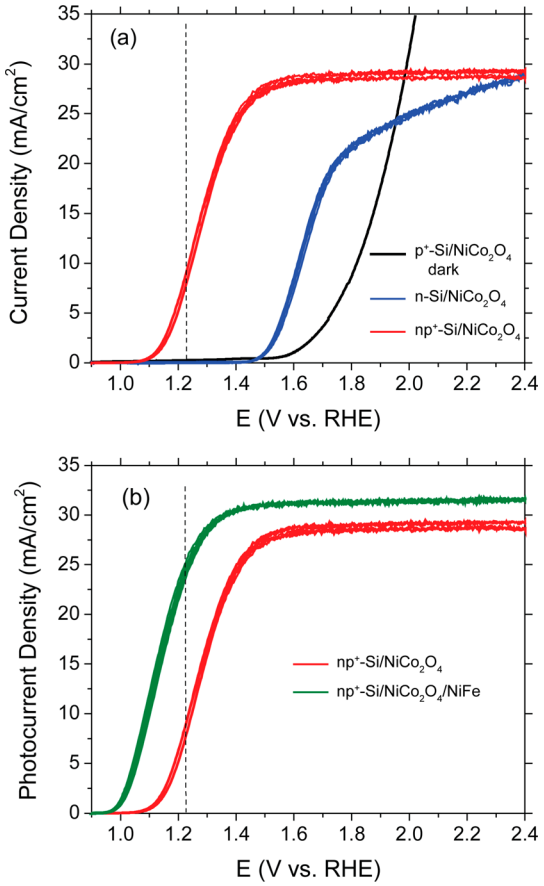

Figure 4. (a) CV scans of p^+ Si, n-Si, and np^+ Si protected with a 40 nm film of p-type $NiCo_2O_4$. The measurements were performed in 1 M KOH (pH 14) with simulated sunlight (no illumination for p^+Si sample). (b) CV scans of $NiCo_2O_4$ coated np^+ Si with (dark green) and without (red) a 2 nm Ni−Fe (50/50) coating serving as an oxygen evolving catalyst. For this film, the onset potential for OER is 0.95 V vs RHE and the current density at the reversible potential for oxygen evolution is 26 mA cm^{-2}. The vertical dashed line is at 1.23 V vs RHE.

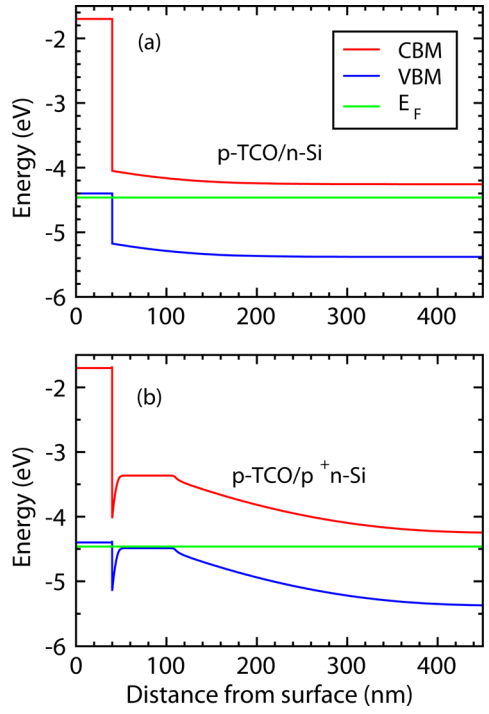

Figure 5. Calculated band diagrams for (a) n-Si/p-$NiCo_2O_4$ and (b) np^+-Si/p-$NiCo_2O_4$. See SI for calculation details.

allowing the photovoltaic properties of the buried junction to be extracted following the procedure of Mills et al.[46] As discussed in detail in the SI, this modeling analysis yields an equivalent open circuit voltage for the Si np junction of about 650 mV, typical for a junction of this type.

The deposition of 2 nm of Ni−Fe as the OER catalyst onto the np^+-Si/$NiCo_2O_4$ enables more efficient transfer of the photogenerated holes from the $NiCo_2O_4$ surface into the electrolyte, as shown by the dark green curve in Figure 4b. The Ni−Fe catalyst reduces the onset potential by 100 mV, to 0.95 V vs RHE, increases the saturation photocurrent density by 10% to over 30 mA/cm^2, and allows for 26 mA/cm^2 at 1.23 vs RHE. This result compares very favorably to other high performance Si-based OER photoanodes reported in the literature.[32,34,47]

Stability of the np^+-Si/$NiCo_2O_4$/NiFe photoanode was evaluated over 72 h by chronoamperometry at 1.4 V vs RHE as shown in Figure 6a. The photocurrent density remains stable and above 30 mA/cm^2 during the entire testing period. During the first 8 h of testing, the incident light was blocked several times to evaluate if corrosion is induced or accelerated by abrupt light intensity changes. We find that the photoanode structure is stable under illumination cycling, with no significant change observed. Figure 6b shows the CVs at the beginning, at the end of a 24 h testing period, and at the end of the complete 72 h testing period. A comparison of these CV curves reveals no performance degradation after 24 h and only a slight decrease of fill factor and shift in the onset potential at the completion of the test. We also performed 24 h stability testing of n-Si/$NiCo_2O_4$ and p^+-Si/$NiCo_2O_4$ structures, which exhibit similarly stable operational behavior, as detailed in Figures S8 and S9.

Sensitive examination of the electrolyte before and after the 72 h test was performed using ICP-MS, which has ppt level detection limits for the elements in the catalyst and protection layer (Ni, Co, and Fe). The results are summarized in Table S2. Given reports that Fe contamination is difficult to avoid in PEC testing, we concentrated on Ni and Co.[48] There was a slight increase in the Ni concentration in the electrolyte, while the Co concentration was nearly unchanged (0.60 vs 0.63 ppb) after the stability test. We primarily attribute these changes to some loss or degradation of the Ni−Fe catalyst, consistent with the small loss in fill factor. This was confirmed by operating a np^+-Si/40 nm $NiCo_2O_4$/Ni−Fe structure at +1.23 V vs RHE until a noticeable change in the CV trace was observed. Reapplication of the NiFe cocatalyst restored the CV trace to the original form (Figure S14).

These findings suggest that the protection layer remains stable even after extended water oxidation. This was demonstrated by long-term testing of a np^+-Si/40 nm $NiCo_2O_4$ structure without the NiFe catalyst. As shown in Figures S12 and S13, this structure is stable for at least 102 h with essentially identical CVs at the beginning and end of the test and a stable photocurrent in time. Examination of the electrolyte after this test found only very small increases in Ni and Co (Table S3), suggesting that the loss of $NiCo_2O_4$ was <0.1 nm during the testing period.

We further examined the structural stability of $NiCo_2O_4$ by *in situ* Raman spectroscopy to determine if repeated cycling/

DOI: 10.1021/jacs.5b03536
J. Am. Chem. Soc. 2015, 137, 9595−9603

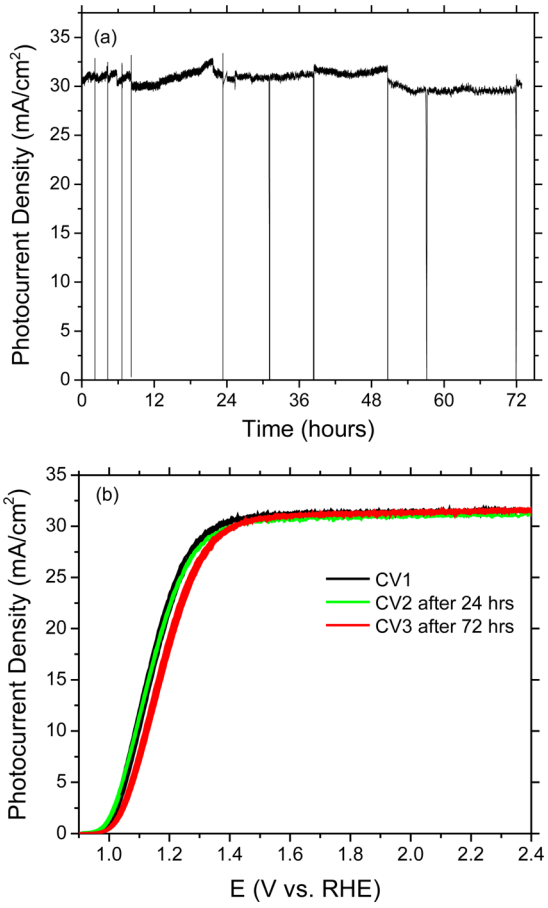

Figure 6. Stability testing of the np$^+$-Si/40 nm $NiCo_2O_4$/Ni–Fe photoanode performed with simulated sunlight at pH 14: (a) photocurrent measured at a bias of 1.4 V vs RHE for a 72 h test; (b) CV scans measured at the start of the test, after 24 h, and after 72 h. The reduced fill factor after 72 h is attributed to loss of the NiFe catalyst (see text).

anodic bias would lead to changes in the overall structure of the p-TCO layer. Films of $NiCo_2O_4$ were deposited on Au electrodes (the standard electrode for *in situ* Raman study) using the same reactive sputtering conditions used for the Si photoanodes. Figure 7 shows *in situ* Raman spectra of $NiCo_2O_4$ with concurrent electrochemical oxidation (1 mV/s) both before and after 16 h of electrochemical cycling from 0 to 0.7 V vs after electrochemical cycling, a redox couple is observed in the voltammograms at potentials consistent with oxidation/reduction of $Ni(OH)_2$/NiOOH (Figure S20).[49,50] However, even after electrochemical cycling, the film exhibits a broad Raman feature at 459–650 cm^{-1} without applied bias (see SI S19), which is characteristic of an amorphous metal oxide/hydroxide. During the 1 mV/s oxidation scan, Raman peaks at 473 and 552 cm^{-1} appear above the OER equilibrium potential for both samples; these features are characteristic of NiOOH formation.[51−55] However, even after 16 h of electrochemical cycling, the NiOOH modes observed here are weaker and broader compared to those reported for pure NiOOH, indicating high structural disorder within this phase. Apart from the 480 and 560 cm^{-1} bands of NiOOH, we do not detect any additional Raman features, including those at 445–465 or 494 cm^{-1}, as well as higher frequencies of 3581–3668 cm^{-1} (Figure S21), which are characteristic of Ni–O and O–H stretching modes of α- or β-$Ni(OH)_2$, respectively.[50−53,56]

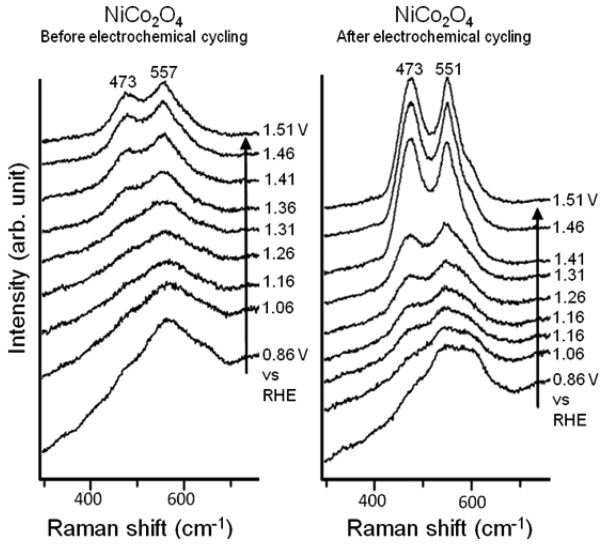

Figure 7. *In situ* Raman spectra for an as-grown $NiCo_2O_4$ film on a Au substrate during a 1 mV/s oxidation scan in 0.1 M KOH as a function of potential (vs Hg/O, reported here vs RHE) before and after 16 h electrochemical cycling.

These findings indicate that as grown $NiCo_2O_4$ is stable and does not wholly transform to crystalline, porous $Ni(OH)_2$/NiOOH. In addition, we did not detect any Raman spectral features consistent with other crystalline transformation products, including Co-based (oxy)hydroxide or spinel-type Co_3O_4 or $NiCo_2O_4$ structures.[57−60]

3.3. Role of the Interface between Si and $NiCo_2O_4$. The role of the Si/$NiCo_2O_4$ interfaces was studied by comparing PEC performance before and after annealing the structure. As shown in Figure 3b, annealing the $NiCo_2O_4$ at 400 °C produces a more crystalline layer with a thicker SiO_x interface layer. XRD analysis (Figure S1) and AFM images (Figure S3) also clearly show the formation of a more crystalline $NiCo_2O_4$ structure after annealing. The annealed film has 10–20% lower conductivity, which should not, by itself, lead to appreciably increased series resistance.

Indeed, annealing has a very small effect on the electrochemical properties of $NiCo_2O_4$. We sputter deposited a series of $NiCo_2O_4$ films onto conductive FTO substrates to exclude possible substrate effects from Si and annealed half of the samples at 400 °C. In order to carefully assess and compare the electrochemical behavior of these films, we used Fe-free epoxy and Fe-free 0.1 M KOH, prepared in the method outlined by Trotochaud et al.[48] and performed all experiments in a glass-free electrochemical cell. Figure 8a shows the voltammograms for as-grown (black) vs annealed (green) $NiCo_2O_4$, concentrating on the current density range near OER onset. Both CV curves show a similar late OER onset potential and low current density, consistent with the J–V curve of $NiCo_2O_4$ on p$^+$-Si in Figure 4a. After adding a Ni–Fe catalyst layer, the as-grown (red) and annealed (blue) exhibit nearly identical reduced oxygen evolution onset potential and increased current. Annealing does not appear to affect the hole conduction of $NiCo_2O_4$ films and catalyst integration.

However, when n-Si/p $NiCo_2O_4$ heterojunction structures were annealed in Ar, the PEC performance decreased significantly, as shown in Figure 8b. Moreover, there was no expected recovery of PEC performance, even with the addition of a Ni–Fe catalyst with annealed n-Si/$NiCo_2O_4$ (shown as

DOI: 10.1021/jacs.5b03536
J. Am. Chem. Soc. 2015, 137, 9595–9603

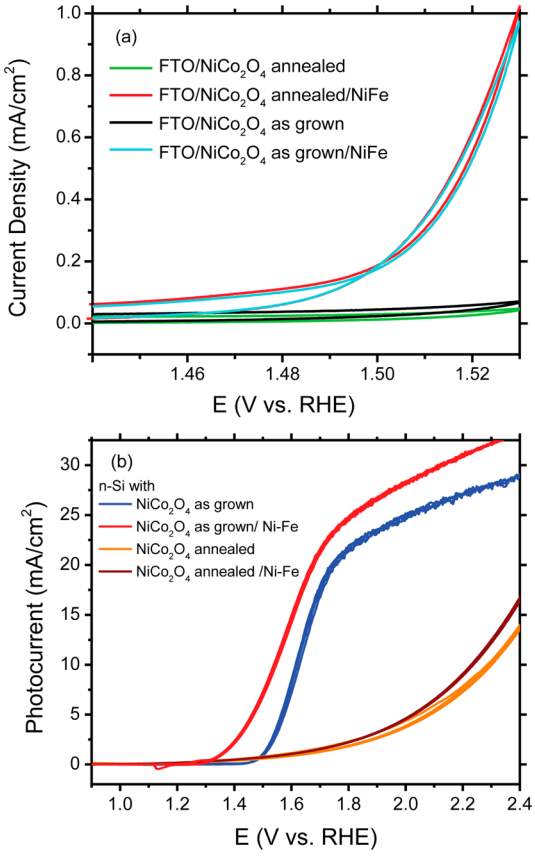

Figure 8. (a) CVs (in dark) of annealed $NiCo_2O_4$ on FTO (green), annealed $NiCo_2O_4$ on FTO catalyzed by NiFe (red), as grown $NiCo_2O_4$ on FTO (black), and as grown $NiCo_2O_4$ on FTO catalyzed by NiFe (light blue) in 0.1 M Fe-free KOH, vs Hg/HgO, converted to RHE, 10 mV/s scan rate. (b) CV scans (under illumination) of as grown $NiCo_2O_4$ on n-Si (blue), as grown $NiCo_2O_4$ on Si with Ni−Fe catalyst (red), annealed $NiCo_2O_4$ on n-Si (orange), and annealed $NiCo_2O_4$ on n-Si with NiFe catalyst (brown).

brown curve in Figure 8b), in contrast to as grown $NiCo_2O_4$ with Ni−Fe (red curve in Figure 8b). As the discussion above has ruled out changes in the hole conduction or surface catalyst integration, we attribute the decreased PEC performance to the creation of a barrier for holes at the interface, leading to increased recombination. The thicker SiO_x region shown in Figure 3b is the likely source of this barrier. We suspect that due to the competition for oxygen between the transition metals and the Si results in the SiO_x layer to grow under the inert gas annealing conditions. A similar effect of decreasing PEC performance was observed by increasing the $NiCo_2O_4$ sputter deposition temperature to 200−400 °C (Figure S18), consistent with the formation of a thicker oxide layer at the interface. The diffusion of oxygen and possibly Ni/Co into SiO_x (shown in Figure 3b) might have also resulted in interface defects which increase the recombination rate of holes at the interface.

3.3. p-TCO Protection of n-InP. To further evaluate the viability of p-TCO protection of semiconductors under illuminated OER conditions, we employed n-InP as a photoanode. In contrast to Si, the native InO_x oxide on InP is conducting. We used the same $NiCo_2O_4$ thickness, 40 nm, as with Si and found that the optimal deposition temperature for PEC performance was 200 °C, safely below the decomposition temperature of InP (about 300 °C). We also note that layers deposited at lower temperatures had poor adhesion. Figure 9 summarizes the PEC testing of n-InP/$NiCo_2O_4$ heterojunction

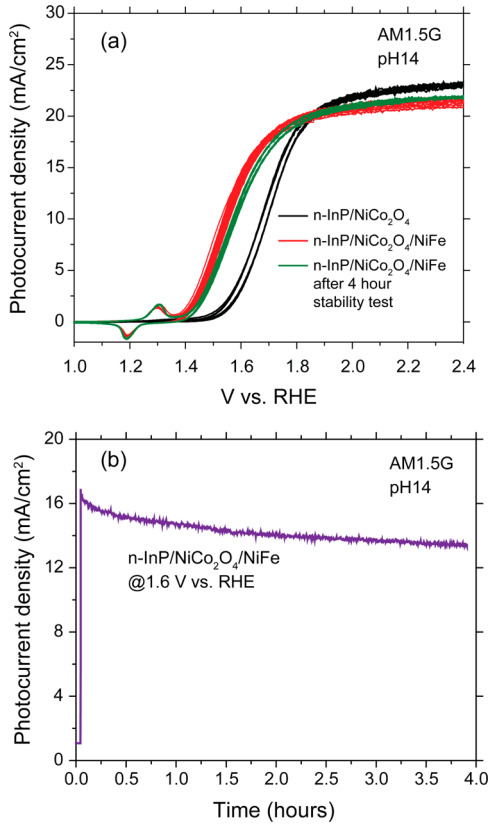

Figure 9. (a) CV scans of n-InP/$NiCo_2O_4$ (black), n-InP/$NiCo_2O_4$/NiFe (red), and n-InP/$NiCo_2O_4$/NiFe after a 4 h stability test. (b) 4 h stability test of a n-InP/p-$NiCo_2O_4$/NiFe heterojunction photoanode.

photoanodes. The onset potential for OER was observed to be approximately 1.55 V vs RHE, with a saturation photocurrent density of about 23 mA/cm^2. After applying Ni−Fe as the OER catalyst, as in the Si case, the onset potential for OER was reduced by almost 200 mV (red curve). A 4 h stability test was also conducted on the sample with Ni−Fe catalyst in 1 M KOH at 1.624 V vs RHE, shown in Figure 9b; the photocurrent declined slightly over this time period. There was a slight anodic shift of the onset potential, Figure 9a. As discussed above for the Si/$NiCo_2O_4$ structures, some of the changes may be due to dissolution of the Ni−Fe catalyst.

5. CONCLUSIONS

Corrosion protection of otherwise unstable photoanode materials (n-Si and n-InP) with a hole-conducting, p-type transparent conducting oxide has been demonstrated. $NiCo_2O_4$ was used as the p-TCO, and this material is shown to have the requisite electronic structure, stability, transparency, and hole conductivity to form efficient water oxidation photoanode heterostructures. Moreover, thin films of this material can be deposited at relatively low temperatures, which can partially avoid the formation of insulating SiO_x layers when Si is used as the light absorber. Excellent PEC performance for water oxidation is demonstrated with an np^+-Si/$NiCo_2O_4$/Ni−Fe structure. *In situ* Raman spectroscopy of $NiCo_2O_4$ is used to evaluate changes in structure which occur under aqueous water oxidation in basic conditions. The relative stability of the

DOI: 10.1021/jacs.5b03536
J. Am. Chem. Soc. 2015, 137, 9595−9603

catalyst and the protection layer was confirmed by photocurrent measurements and ICP-MS measurements of the electrolyte following long-term testing for 72 h. The precise nature of the interface between the semiconductor and the p-TCO is shown to be crucial in achieving high PEC performance. For example, annealing n-Si/p-$NiCo_2O_4$ heterojunction photoanodes produces only very small changes in the $NiCo_2O_4$ but significantly affects the interface structure, leading to a decrease in performance. P-$NiCo_2O_4$ also forms a charge-separating heterojunction with n-InP and leads to stable operation over several hours.

■ ASSOCIATED CONTENT

Supporting Information

Experimental details; detailed characterization; photoelectrochemical measurement details; supplemental stability data, and Faradaic efficiency; additional *in situ* Raman spectroscopy; XPS measurements; *ab initio* calculation of the work function; modeling of PEC data. The Supporting Information is available free of charge on the ACS Publications website at DOI: 10.1021/jacs.5b03536.

■ AUTHOR INFORMATION

Corresponding Author

*JWAger@lbl.gov

Notes

The authors declare no competing financial interest.

■ ACKNOWLEDGMENTS

We thank Raffaella Buonsanti for assistance with SEM imaging, Karl Walczak and Jeffery Beeman for Faradaic efficiency measurements and for processing np-Si wafers, and Prof. Ali Javey's group for providing n-InP wafers. We thank NCEM staff Marissa Libbee and Chengyu Song for generous help on TEM sample preparation and imaging. This material is based upon work performed by the Joint Center for Artificial Photosynthesis, a DOE Energy Innovation Hub, supported through the Office of Science of the U.S. Department of Energy under award no. DE-SC0004993. Characterization work by R.W.R. was supported by the Bay Area Photovoltaic Consortium. Work at the National Center for Electron Microscopy and Molecular Foundry was supported by the Office of Science, Office of Basic Energy Sciences, of the U.S. Department of Energy under contract no. DE-AC02−05CH1123.

■ REFERENCES

(1) Chu, S.; Majumdar, A. *Nature* **2012**, *488* (7411), 294.
(2) Nocera, D. G. *Acc. Chem. Res.* **2012**, *45* (5), 767.
(3) Turner, J. A. *Science (Washington, DC, U. S.)* **2004**, *305* (5686), 972.
(4) Graves, C.; Ebbesen, S. D.; Mogensen, M.; Lackner, K. S. *Renewable Sustainable Energy Rev.* **2011**, *15* (1), 1.
(5) Khaselev, O.; Turner, J. A. *Science (Washington, DC, U. S.)* **1998**, *280* (5362), 425.
(6) Brillet, J.; Cornuz, M.; Formal, F. Le; Yum, J.-H.; Grätzel, M.; Sivula, K. *J. Mater. Res.* **2010**, *25* (01), 17.
(7) Rongé, J.; Bosserez, T.; Martel, D.; Nervi, C.; Boarino, L.; Taulelle, F.; Decher, G.; Bordiga, S.; Martens, J. A. *Chem. Soc. Rev.* **2014**, *43*, 7963.
(8) Nielander, A. C.; Shaner, M. R.; Papadantonakis, K. M.; Francis, S. A.; Lewis, N. S. *Energy Environ. Sci.* **2015**, *8* (1), 16.
(9) Elsenberg, R.; Gray, H. B. *Inorg. Chem.* **2008**, *47* (6), 1697.
(10) Haussener, S.; Xiang, C.; Spurgeon, J. M.; Ardo, S.; Lewis, N. S.; Weber, A. Z. *Energy Environ. Sci.* **2012**, *5* (12), 9922.
(11) Kohl, P. A.; Frank, S. N.; Bard, A. J. *J. Electrochem. Soc.* **1977**, *124* (2), 225.
(12) Parkinson, B. *Acc. Chem. Res.* **1984**, *17* (12), 431.
(13) McKone, J. R.; Lewis, N. S.; Gray, H. B. *Chem. Mater.* **2014**, *26* (1), 407.
(14) Liu, R.; Zheng, Z.; Spurgeon, J.; Yang, X. *Energy Environ. Sci.* **2014**, *7* (8), 2504.
(15) Gerischer, H. *J. Electroanal. Chem. Interfacial Electrochem.* **1977**, *82* (1−2), 133.
(16) Chen, S.; Wang, L.-W. *Chem. Mater.* **2012**, *24* (18), 3659.
(17) Kraft, A.; Gorig, B.; Heckner, K. H. *Sol. Energy Mater. Sol. Cells* **1994**, *32* (2), 151.
(18) Seger, B.; Castelli, I. E.; Vesborg, P. C. K.; Jacobsen, K. W.; Hansen, O.; Chorkendorff, I. *Energy Environ. Sci.* **2014**, *7* (8), 2397.
(19) Sun, K.; Saadi, F. H.; Lichterman, M. F.; Hale, W. G.; Wang, H.-P.; Zhou, X.; Plymale, N. T.; Omelchenko, S. T.; He, J.-H.; Papadantonakis, K. M.; Brunschwig, B. S.; Lewis, N. S. *Proc. Natl. Acad. Sci. U. S. A.* **2015**, 201423034.
(20) Campet, G.; Puprichitkun, C.; Sun, Z. W. *J. Electroanal. Chem. Interfacial Electrochem.* **1989**, *269* (2), 435.
(21) Chen, Y. W.; Prange, J. D.; Duhnen, S.; Park, Y.; Gunji, M.; Chidsey, C. E. D.; McIntyre, P. C. *Nat. Mater.* **2011**, *10* (7), 539.
(22) Scheuermann, A. G.; Prange, J. D.; Gunji, M.; Chidsey, C. E. D.; McIntyre, P. C. *Energy Environ. Sci.* **2013**, *6* (8), 2487.
(23) Yang, X.; Liu, R.; Du, C.; Dai, P.; Zheng, Z.; Wang, D. *ACS Appl. Mater. Interfaces* **2014**, *6* (15), 12005.
(24) Sun, Z. W.; Campet, G. *Mater. Sci. Eng., B* **1990**, *5* (4), 455.
(25) Hu, S.; Shaner, M. R.; Beardslee, J. A.; Lichterman, M.; Brunschwig, B. S.; Lewis, N. S. *Science (Washington, DC, U. S.)* **2014**, *344* (6187), 1005.
(26) Greiner, M. T.; Helander, M. G.; Tang, W. M.; Wang, Z. B.; Qiu, J.; Lu, Z. H. *Nat. Mater.* **2011**, *11* (1), 76.
(27) Fortunato, E.; Barquinha, P.; Martins, R. *Adv. Mater.* **2012**, *24* (22), 2945.
(28) Ginley, D. S.; Bright, C. *MRS Bull.* **2000**, *25* (08), 15.
(29) Banerjee, A. N.; Chattopadhyay, K. K. *Prog. Cryst. Growth Charact. Mater.* **2005**, *50* (1−3), 52.
(30) Stadler, A. *Materials* **2012**, *5* (4), 661.
(31) Fortunato, E.; Ginley, D.; Hosono, H.; Paine, D. C. *MRS Bull.* **2007**, *32*, 242.
(32) Yang, J.; Walczak, K.; Anzenberg, E.; Toma, F. M.; Yuan, G.; Beeman, J.; Schwartzberg, A.; Lin, Y.; Hettick, M.; Javey, A.; Ager, J. W.; Yano, J.; Frei, H.; Sharp, I. D. *J. Am. Chem. Soc.* **2014**, *136* (17), 6191.
(33) Sun, K.; Shen, S.; Cheung, J. S.; Pang, X.; Park, N.; Zhou, J.; Hu, Y.; Sun, Z.; Noh, S. Y.; Riley, C. T.; Yu, P. K. L.; Jin, S.; Wang, D. *Phys. Chem. Chem. Phys.* **2014**, *16* (10), 4612.
(34) Mei, B.; Permyakova, A. A.; Frydendal, R.; Bae, D.; Pedersen, T.; Malacrida, P.; Hansen, O.; Stephens, I. E. L.; Vesborg, P. C. K.; Seger, B.; Chorkendorff, I. *J. Phys. Chem. Lett.* **2014**, *5* (20), 3456.
(35) Sun, K.; McDowell, M. T.; Nielander, A. C.; Hu, S.; Shaner, M. R.; Yang, F.; Brunschwig, B. S.; Lewis, N. S. *J. Phys. Chem. Lett.* **2015**, *6* (4), 592.
(36) Singh, D. *J. Electrochem. Soc.* **1998**, *145* (1), 116.
(37) Yuan, Y. F.; Xia, X. H.; Wu, J. B.; Yang, J. L.; Chen, Y. B.; Guo, S. Y. *Electrochim. Acta* **2011**, *56* (6), 2627.
(38) Lin, F.; Boettcher, S. W. *Nat. Mater.* **2013**, *13* (1), 81.
(39) Windisch, C. F., Jr; Ferris, K. F.; Exarhos, G. J.; Sharma, S. K. *Thin Solid Films* **2002**, *420−421*, 89.
(40) Alcántara, R.; Jaraba, M.; Lavela, P.; Tirado, J. L. *Chem. Mater.* **2002**, *14* (7), 2847.
(41) Wei, T. Y.; Chen, C. H.; Chien, H. C.; Lu, S. Y.; Hu, C. C. *Adv. Mater.* **2010**, *22* (3), 347.
(42) Li, J.; Xiong, S.; Liu, Y.; Ju, Z.; Qian, Y. *ACS Appl. Mater. Interfaces* **2013**, *5* (3), 981.
(43) Kawazoe, H.; Yasukawa, M.; Hyodo, H.; Kurita, M.; Yanagi, H.; Hosono, H. *Nature* **1997**, *389* (6654), 939.

DOI: 10.1021/jacs.5b03536
J. Am. Chem. Soc. 2015, 137, 9595−9603

(44) Klein, A.; Körber, C.; Wachau, A.; Säuberlich, F.; Gassenbauer, Y.; Harvey, S. P.; Proffit, D. E.; Mason, T. O. *Materials* **2010**, *3* (11), 4892.
(45) Hautier, G.; Miglio, A.; Ceder, G.; Rignanese, G.-M.; Gonze, X. *Nat. Commun.* **2013**, *4*, 2292.
(46) Mills, T. J.; Lin, F.; Boettcher, S. W. *Phys. Rev. Lett.* **2014**, *112* (14), 148304.
(47) Kenney, M. J.; Gong, M.; Li, Y.; Wu, J. Z.; Feng, J.; Lanza, M.; Dai, H. *Science* **2013**, *342* (6160), 836.
(48) Trotochaud, L.; Young, S. L.; Ranney, J. K.; Boettcher, S. W. *J. Am. Chem. Soc.* **2014**, *136* (18), 6744.
(49) Lyons, M. E. G.; Brandon, M. P. *Int. J. Electrochem. Sci.* **2008**, *3* (12), 1386.
(50) Kostecki, R. *J. Electrochem. Soc.* **1997**, *144* (2), 485.
(51) Cornilsen, B. C.; Karjala, P. J.; Loyselle, P. L. *J. Power Sources* **1988**, *22*, 351.
(52) Desilvestro, J. *J. Electrochem. Soc.* **1988**, *135* (4), 885.
(53) Johnston, C.; Graves, P. R. *Appl. Spectrosc.* **1990**, *44* (1), 105.
(54) Yeo, B. S.; Bell, A. T. *J. Phys. Chem. C* **2012**, *116* (15), 8394.
(55) Louie, M. W.; Bell, A. T. *J. Am. Chem. Soc.* **2013**, *135* (33), 12329.
(56) Bernard, M. C.; Bernard, P.; Keddam, M.; Senyarich, S.; Takenouti, H. *Electrochim. Acta* **1996**, *41* (1), 91.
(57) Pauporté, T.; Mendoza, L.; Cassir, M.; Bernard, M. C.; Chivot, J. *J. Electrochem. Soc.* **2005**, *152* (2), C49.
(58) Tang, C. W.; Wang, C. Bin; Chien, S. H. *Thermochim. Acta* **2008**, *473* (1−2), 68.
(59) Yang, J.; Liu, H.; Martens, W. N.; Frost, R. L. *J. Phys. Chem. C* **2010**, *114* (1), 111.
(60) Iliev, M. N.; Silwal, P.; Loukya, B.; Datta, R.; Kim, D. H.; Todorov, N. D.; Pachauri, N.; Gupta, A. *J. Appl. Phys.* **2013**, *114* (3), 033514.

DOI: 10.1021/jacs.5b03536
J. Am. Chem. Soc. 2015, 137, 9595−9603